

Rational Design and Synthesis of a Novel BODIPY-based Probe for Selective Imaging of Tau Tangles in Human iPSC-derived Cortical Neurons

Alessandro Soloperto

Istituto Italiano di Tecnologia

Deborah Quaglio

Sapienza University of Rome

Paola Baiocco

Sapienza University of Rome

Isabella Romeo

Istituto Italiano di Tecnologia

Mattia Mori

University of Siena

Matteo Ardini

University of L'Aquila

Caterina Presutti

Sapienza University of Rome

Ida Sannino

Istituto Italiano di Tecnologia

Silvia Ghirga

Istituto Italiano di Tecnologia

Antonia Iazzetti

Catholic University of Sacred Heart

Rodolfo Ippoliti

University of L'Aquila

Giancarlo Ruocco

Istituto Italiano di Tecnologia

Bruno Botta

Sapienza University of Rome

Francesca Ghirga

Sapienza University of Rome

Silvia Di Angelantonio (✉ silvia.diangelantonio@uniroma1.it)

Sapienza University of Rome

Alberto Boffi

Research Article

Keywords: BODIPYs, Alzheimer's disease, tau protein, NFTs, NIRF, fluorescence imaging, diagnosis, microscopy

Posted Date: December 6th, 2021

DOI: <https://doi.org/10.21203/rs.3.rs-1117010/v1>

License:   This work is licensed under a Creative Commons Attribution 4.0 International License.
[Read Full License](#)

Abstract

Numerous studies have shown a strong correlation between the number of neurofibrillary tangles of the tau protein and Alzheimer's disease progression, making the quantitative detection of tau very promising from a clinical point of view. However, the lack of highly reliable fluorescent probes for selective imaging of tau neurofibrillary tangles is a major challenge due to sharing similar β -sheet motifs with homologous Amyloid- β fibrils. In the current work, we describe the rational design and the in silico evaluation of a small-size focused library of fluorescent probes, consisting of a BODIPY core (electron acceptor) featuring highly conjugated systems (electron donor) with a length in the range 13-19 Å at C3. Among the most promising probes in terms of binding mode, theoretical affinity and polarity, BT1 has been synthesized and tested in vitro onto human induced pluripotent stem cells derived neuronal cell cultures. The probe showed excellent photophysical properties and high selectivity allowing in vitro imaging of hyperphosphorylated tau protein filaments with minimal background noise. Our findings offer new insight into the structure-activity relationship of this class of tau selective fluorophores, paving the way for boosting tau tangle detection in patients possibly through retinal spectral scans.

Introduction

Alzheimer's disease (AD) is a neurodegenerative disorder responsible for more than 80% of cases of senile dementia. Despite the presence of extracellular β -amyloid ($A\beta$) and intracellular tau protein aggregates is an established hall-mark of the AD pathology, the limited scientific evidence on the timing of the molecular cascade leading to AD-related neurodegeneration has made difficult the development of both early diagnostic strategies and effective therapies.

To date, no solutions have been found to date that clearly hinders disease progression thus improving the life quality of patients and caregivers. Moreover, most of the drugs developed in rodent AD models failed in reducing disease burden in clinical trials, likely due to the lack of globally recognized diagnostic criteria in pre-symptomatic phases of AD^{1,2}. Indeed, the only drug recently approved by FDA, Aducanumab, has been shown to reduce $A\beta$ plaques in people showing early Alzheimer's disease together with evident buildup of $A\beta$ plaques. Moreover, Aducanumab, has been approved, despite a number of side effects including amyloid-related imaging abnormalities, headache, dizziness, nausea, confusion and vision changes.

Consequently, the current challenge is the development of non-invasive in vivo approaches that can ensure the assessment of small, still undetectable, neuropathological changes in living patients. Indeed, to date, a definitive diagnosis for AD can be made only post-mortem, by immunohistochemical analysis of brain samples³.

Thus, numerous efforts are now exploiting cerebrospinal fluid analysis (CSF)⁴ and cutting-edge diagnostic neuroimaging techniques⁵, for the detection of the presence of $A\beta$ and/or tau protein aggregates in living AD patients. However, despite being relatively specific and selective, these

approaches display several limitations including high costs of management and invasiveness. In 2018, the National Institute on Aging and Alzheimer's Association confirmed a biological definition of AD and established a consensus on bioprobe-based diagnostic criteria for interventional research⁶. Three main biomarkers have been identified for AD, namely: i) the A β 42 peptide, which is the main component of the toxic A β plaques; ii) the coupled units of hyperphosphorylated tau protein (P-tau) and total-tau monomers (T-tau) which are the key bricks of the neurofibrillary tangles (NFTs).

The amyloid cascade hypothesis, the A β hypothesis, has been the mainstream explanation for the AD pathogenesis for over 25 years⁷; however, except for Aducanumab, all attempts to develop A β -targeting drugs to treat AD failed in clinical trials, thus suggesting that A β cannot be considered as main the factor underlying the development and progression of AD. It has to be considered that the A β hypothesis, involving intracellular β and γ secretases, is consistent with familial AD cases, where pathogenetic mutations of APP are clustered near the cleavage sites of secretases, and are associated with an increase in the ratio of A β 42 formation. Interestingly, Down's syndrome patients with trisomy 21 exhibit AD-like pathology by about 40 years of age⁸. In addition, other familial AD mutations, identified in presenilin 1/2, which is a component of γ -secretase, are closely linked to the A β production process, providing a rational basis for the idea that A β amyloid fibril formation can account for the familial AD pathogenesis⁷. However, although transgenic mice expressing familial AD mutations on these genes display accumulation of A β plaques, intracellular tau tangles, and neuronal death have not been observed in their brains⁹. Indeed, the only AD mouse model characterized by tau pathology is a triple transgenic mouse expressing specifically in the MAPT gene the P301L mutation, which, in patients, relates to familial frontotemporal dementia (3xTg-AD mouse)^{10,11}. Thus, it is now accepted that extra-cellular accumulation of A β fibrils does not induce tau accumulation; consistently, antibody-based pharmacological treatments targeting A β in AD mice decreased brain A β deposition, leaving unaltered tau accumulation¹²⁻¹⁵. Strikingly, the detection of A β amyloid accumulation in the living patient's brain with recent imaging tools, showed AD patients with little amyloid deposits, while elderly non-demented patients with a distribution of senile plaques as extensive as that of dementia patients¹⁶⁻¹⁸. Based on this evidence, the amyloid hypothesis of neurodegeneration/neuronal loss and amyloid deposition appear to be independent phenomena¹⁸.

On the other hand, numerous studies have shown a more rigorous correlation between the number of neurofibrillary tangles of the tau protein and disease progression, making the quantitative detection of tau very promising from a clinical point of view¹⁹. Moreover, this could be useful for disease prediction and staging as well as for the evaluation of the effectiveness of medical treatments. Therefore, tau visualization on a temporal and spatial scale has the potential to become a prognostic tool. To address this issue, positron emission tomography (PET) imaging exploits isotope-conjugated tracers that bind tau molecules with high affinity and specificity. However, the structural organization and the intracellular localization of tau protein constitute a huge challenge for the development of reliable radio-tracers^{20,21}.

Over the last decade, significant progress has been made in the field of small molecule fluorescent sensors for targeting aggregated tau^{22,23}. The main detection strategy has been based on the development of probes intercalating into P-tau aggregates²⁴. The design of NFT binders has been guided by two hypotheses: i) probes having a distance of 13–19 Å between the donor and acceptor selectively target NFTs, while probes characterized by a shorter distance favor the detection of Aβ plaques; ii) fused ring containing probes show higher selectivity for tau over Aβ fibrils. However, due to the intrinsically disordered nature of NFTs, a clear structure–activity relationship for tau protein has not been identified to date, making the rational design of specific fluorescence probes challenging.

Indeed, one major concern is represented by the nonspecific binding of developed ligands due to the presence of β-sheet motifs, a common feature of protein aggregates other than NFTs (such as TDP-43 and α-synuclein). Moreover, heterogeneous structural organization of tau aggregates has been observed in AD and non-AD-related tauopathies. Thus, the need for non-toxic fluorescence dyes bearing better selectivity, affinity, and specificity for tau proteins is fostering the development of a novel generation of tracers^{25,26}. In this regard, the recent characterization of tau protein structure at the atomic^{27,28} might represent an outstanding milestone for better tackling such needs²⁹.

A novel approach consists in the development of compounds based on boron dipyrin platform (4,4-difluoro-4-bora-3a,4a-diaza-s-indacene, also known as BODIPY) that are endowed with spectroscopic and photodynamic features that can be easily customized through relatively simple chemical reactions thus making them suitable for several applications³⁰. Based on molecular docking observations, the synthesis of two BODIPY-based probes selective for tau (TAU1 and Tau2) has been described³¹. Specifically, TAU1 has been reported to label P-tau in the 3xTg-AD mouse model, opening up avenues for the cost-effective monitoring of the tau protein aggregation state in animal models and possibly in human fixed tissue staining³¹. Recently, the development of non-toxic tau tracers suitable for in vivo applications is also boosted by clinical evidence showing the presence of tau aggregates in postmortem samples of AD patients' retina^{32–35}. Indeed, the retinal imaging of tau aggregates in living patients could play a dramatic role in AD diagnosis^{35,36}, and BODIPY based probes may represent a valuable tool for this purpose. However, chemical aspects such as binding selectivity, short emission wavelength and poor solubility must be taken into account, as they represent a clear obstacle to overcome for further human biomedical application. Concerning the use of chemicals for diagnostic and therapeutic purposes in human patients, it has to be considered that the failure of pre-clinical trials of most of the potential drug candidates, today screened on AD mouse models³⁷, arises also from physiological and evolutionary species-specific differences that hamper translating to humans the results obtained in rodents. Therefore, the need to develop a humanized AD model is rapidly growing, and would aid to better understand the molecular cascade and thus accelerate the screening process for diagnostic and therapeutic candidate molecules. In this framework, human-induced Pluripotent Stem Cells (hiPSCs)³⁸ have emerged, in the last decade, as useful tools for modeling human neurological disorders, including AD. Indeed, by introducing specific disease-causing genomic alterations into the hiPSC line of choice by gene editing, and differentiating

iPSCs into the neuronal, glial, or retinal cells, it is possible to provide a straightforward approach for unmasking phenotypic and functional alterations characteristic of complex diseases.

We here describe the rational design of a small-size focused library of fluorescent probes, to target P-tau, consisting of a BODIPY core functionalized in position C3 with a highly conjugated system ending with an amino group, and characterized by a distance in the range 13-19 Å between the electron donor and the acceptor portion. The interaction between the aforementioned BODIPY series and the crystallographic structures 27 of the hexapeptide fragment PHF6, present in the R3 region of the P-tau protein and responsible for the propensity of the protein itself to assemble into fibrils, has been studied by molecular docking. Such a study indicated hit compounds within the in silico generated collection. The most promising probe in terms of binding mode and theoretical affinity, BT1, has been synthesized and tested in vitro onto human iPSC-derived NGN2-induced neuronal cell cultures after 30 days in culture. The probes showed excellent photophysical properties and high selectivity allowing in vitro imaging of hyperphosphorylated tau protein filaments with minimal background noise. This study provides new insights into the structure-activity relationship of this class of tau selective fluorophores.

Results

- **Rational design of a small-size focused library of BODIPY fluorescent probes selective for NFTs.**

Currently, a pharmacophoric model for the interaction between fluorescent probes and NFTs has not been defined and potential selective probes characterized by high chemical diversity have been identified. However, these compounds have several common structural features that allow defining some guidelines for the rational design of new probes²². Based on these, a small-size focused library of eight new BODIPY probes, BT1-8 (Figures 1 and Supplementary Figure S1), has been designed by extending the conjugation of position 3 of the BODIPY core characteristic of a known selective fluorescent probe, TAU1 (Figure 1), in order to gain new insights into the structure-activity relationship of this fancy class of fluorophores. The series of fluorescent probes here designed, consisted of a BODIPY core functionalized in position 3 with a highly conjugated system ending with an aliphatic amine, cyclic and non, or aromatic, characterized by a distance between the electron donor portion and the acceptor portion of 13-19 Å, to improve the P-tau vs Aβ selectivity, and by a different polarity

- **Molecular docking.**

The detection strategy for NFTs is not as clear as it is for Aβ aggregates, probably due to the less defined binding modes in the case of P-tau aggregates. The most challenging aspect of the approach based on the intercalation of a selective probe is to ensure selective binding affinity toward P-tau aggregates over Aβ plaques. To overcome this issue, in silico pre-screening of the chemical library was carried out to prioritize a few compounds for chemical synthesis and biological testing, based on their predicted binding mode and theoretical affinity for the target protein. Following the work of Verwilt et al, the small library of BODIPY-based probes was docked toward the 6-mer model of the PHF6 fragment, present in the

R3 region of the P-tau protein and responsible for the propensity of the protein itself to assemble into fibrils³¹. Docking was analyzed both in terms of binding mode and theoretical affinity with the aim of identifying the most promising molecule as a selective P-tau probe (Figure 1, Supplementary Figures S1-10, and Supplementary Table 1). All the tested molecules were able to interact with the protein system in silico, and to fit the cavity formed by the assembly of multiple polypeptide units. In particular, the fluorescent moiety of the compounds was mostly docked into the central part of the binding site, suggesting that it has a preference for lipophilic regions of the target protein, while the aliphatic chain was projected towards the entrance of the lipophilic tunnel (Supplementary Figures S2-S10). The docking of the BT5, BT7, and BT8 (pose 2) compounds in their protonated form provided a weaker theoretical binding affinity than other neutral compounds (see Supporting Information, Table 1) probably due to the electrostatic repulsion between the protonated ligands' moiety and the positively charged N-terminal ends of valine residues that are exposed within the accessible side of the protein tunnel.

BT2 provided a better theoretical binding affinity than other probes, but it presented two statistically most relevant docking poses in which the BODIPY core binds with opposite orientation near the entrance of the lipophilic tunnel. Indeed, in the second pose the aliphatic chain ending with a bulky hydrophobic diphenylamine amine is project-ed deeply in the central part of the receptor. Accordingly, combining the predicted affinity and binding mode with the polarity, we decided to synthesize the BT1 compound and to investigate its selectivity towards the neurofibrillary aggregates of P-tau protein in vitro onto iPSC-derived NGN2-induced neuronal cell cultures after 30 days in culture.

- **Synthesis and Fluorescence of BT1.**

The BT1 compound was found to be the most promising compound as a selective marker of the P-tau protein NFTs in terms of in silico affinity, binding conformation and polarity. An efficient and versatile two-step synthetic strategy was developed (Figure 2). BT1 was synthesized via a Knoevenagel condensation between the selected and commercially available BODIPY core (4) and the trans-4- [2- (4-dimethylaminophenyl) vinyl] benzaldehyde (3). The latter was synthesized by Heck reaction between 4-bromobenzaldehyde (1) and 4-dimethylaminostyrene (2), both commercially available, in the presence of a catalyst suitably chosen to promote the stereoselectivity of the reaction. The characterization of all new final products by ¹H and ¹³C NMR, as well as ESI-MS, can be found in the Supplementary Information (Supplementary Figures S11-S16). BT1 has successfully dissolved up to 11 mM concentration in DMSO and accordingly diluted in the PBS buffer. Fluorescence emission bands of BT1 at a final concentration of 100 μM in PBS were analyzed and compared to the emission bands of the purchased fluorescent probe TAU1. In our hands, TAU1 showed an emission band at 510 nm when excited at a wavelength in the range 420-475 nm. On the contrary, BT1 showed a red-shifted intense band with a maximum at about 565 nm using an excitation wavelength at 520 nm (Figure S18). The fluorescence spectra of BT1 in the presence of preincubated tau fibrils were monitored revealing a strong enhancement at 565 nm in agreement with the formation of elongated fibrils of Tau protein as confirmed by TEM im-ages performed under the same experimental conditions (Figure S19).

- **Validation of human-induced pluripotent cell line WT#1 and neuronal differentiation.**

An in-house iPSC line named WT#1 (Supplementary Figure S17)^{39,40} was used for assessing the detection efficiency of tau aggregates by BT1 compound. The iPSC line WT#1 carries the doxycycline-inducible NGN2 cassette into the safe harbor AAVS1 locus⁴¹. NGN2-engineered iPSCs were treated for 4 days with 2 ug/mL doxycycline for inducing the rapid overexpression of the human NGN2 gene which is recognized as a potent molecular factor capable to drive the differentiation towards a neurocortical fate and specifically towards excitatory cortical neurons (Figure 3A, B).

To confirm the proper differentiation of WT#1 line into neuronal cells after 30 days in culture (Figure 3C), a time-course quantification by real-time PCR of the key neuronal molecular markers was performed. As expected, a steep increase of NGN2 transcript was found in the first week of culture as a consequence of the doxycycline treatment, together with the expression of PAX6 transcript, an early neural progenitor marker. Moreover, as maturation proceeded, NGN2 transcript level decreased in favor of dorsocortical and pan-neuronal markers FOXG1, TUJ1, MAP2. Excitatory synaptic transcripts (SYN and vGLUT1) arose in a time-dependent fashion between day 15 and day 30, suggesting the establishment of a mature neuronal network at later time points. At 30 days in culture, neuronal maturation was also evaluated at the protein level by confocal immunofluorescence analysis, confirming the expression of NeuN, TUJ1, and MAP2 neuronal markers (Figure 3D) as well as T-tau expression (Figure 3E), which showed the presence of a dense and ramified neuronal network.

- **BT1 probe shows improved in vitro specificity for AT8-positive tau aggregates.**

With the aim to generate an in vitro model of tau hyperphosphorylation and neuronal degeneration, iPSC-derived NGN2 neuronal cultures were treated for 2 hours with 50 nM okadaic acid (OA), a potent inhibitor of many biological processes including the serine/threonine phosphatases, to induce protein hyperphosphorylation, and specifically to enhance the phosphorylation of endogenous neuronal tau protein. The effect of OA treatment was evaluated measuring the fluorescence signal intensity of both P-tau and oligomeric tau protein, two biological markers associated with AD related neuronal degeneration, using the specific AT8 and T22 antibodies respectively.

To characterize the ability of BT1 to detect different forms of tau proteins, control and OA-treated neuronal cultures were incubated BT1 probe (100 μ M; Figure 4A) for 30 minutes at 37°C and then fixed and immunolabeled using AT8 and T22. Fluorescence signals were acquired through a spinning-disk confocal microscope equipped with conventional filters and a filter set specific for the spectra obtained for BT1 (excitation wavelength 520 nm, emission wavelength: 560/40 nm) at the concentration used on neuronal cultures (Supplementary Figure S18A.).

Parallel experiments were performed using the TAU1 probe (100 μ M; Figure 4B), acquired using the excitation and emission wavelengths reported in Supplementary Figure S18B, in combination with AT8 and T22.

The acquired images were analyzed through a custom made MATLAB code capable of simultaneously performing image background correction, antibody dot-like signal detection and finally fluorescence intensity quantification and channel colocalization (see Methods section and Figure 6)

As shown in Figure 5A, OA treatment increased the expression of both P-tau and oligomeric tau in human iPSC-derived neurons, confirming the establishment of a neurotoxic condition within the neuronal networks. The quantified data, reported in Figure 5, showed that both BODIPY based probes bind to P-tau and oligomeric tau, as shown by colocalization with AT8 and T22 respectively. Strikingly, BT1 displayed improved detection of AT8-positive P-tau tangles when compared to TAU1, as demonstrated by the higher Mander's (Figure 5B) and Pearson's (Figure 5C) correlation indexes in OA treated human neurons

Discussion

We here report the synthesis of a novel BODIPY based fluorophore developed to bind hyperphosphorylated and oligomeric tau, and its characterization in vitro and in a humanized model of cortical neurons.

We combined synthetic organic chemistry and computational modelling, biochemistry and molecular and cellular biology in a concerted multidisciplinary strategy to developed fluorescent sensors for selectively targeting neurofibrillary tangles (NFTs) of the tau protein which could represent a valuable tool in Alzheimer's disease (AD) diagnosis. The BODIPY core emerged as privileged scaffold in the design of cross β -sheet fluorescent binders, based on molecular modeling predictions and prior studies. Here, we designed a small-size focused library of fluorescent probes consisting of a BODIPY core (electron acceptor) featuring a highly conjugated system ending with an aliphatic amine (electron donor) with a length in the range 13-19 Å, and characterized by a different polarity. This structural modification were rationally designed to improve the P-tau vs A β selectivity respect to TAU1, that has been shown to bind also A β ⁴², and the small-size focused library was docked toward the 6-mer model of the PHF6 fragment, present in the R3 region of the P-tau protein and responsible for the propensity of the protein itself to assemble into fibrils. Among the most promising probes in terms of binding mode, theoretical affinity and polarity, BT1 has been synthesized and tested in vitro onto human iPSC-derived NGN2-induced neuronal cell cultures, which represent a reliable system for modeling human neurological disorders, including AD. The probe BT1 was prepared via an efficient and cost-effective two-step synthetic strategy and exhibited excellent photophysical properties. The probe was clearly able to efficiently provide in vitro imaging of hyperphosphorylated tau protein filaments with minimal background noise and high selectivity. The designed BODIPY based BT1 compound improved the detection of P-tau and thus tau tangles in cortical neurons, and displayed a higher colocalization with the commercial available Phospho-Tau Antibodies AT8 when compared to the reference probe TAU1³¹.

It has to be noticed that while previous reports^{31,42}, indicated that the emission wavelength of TAU1 is >650 nm, prior to perform measurements on iPSC derived cortical neurons we measured excitation/emission spectra for both BT1 and TAU1 using the experimental conditions suitable for

neuronal tau imaging and we found different results. This discrepancy may arise from different solution buffer conditions. Indeed, we measured excitation/emission spectra of TAU1, first dissolved in 100% DMSO and then diluted in PBS to reach a final concentration of 100 μ M (DMSO 1%), suitable to be used in living cells. In these condition no peaks were detected at 660 nm (see Supplementary Figure 18), a wavelength reported for TAU1 dissolved in chloroform and in the presence of tau protein^{31,42}.

Strikingly, the optimized compound can be used on human living tissue. Moreover, given the wide chemical versatility of the BODIPY scaffold, owing to their relative ease of substitution and generally highly fluorescent nature, our findings offer new insight into the structural optimization of specific compounds for different target proteins, helping in the differential diagnosis of neurodegenerative diseases associated with the deposition of protein aggregates.

Methods

Materials. Compound TAU1 was purchased from SYNCOM (custom synthesis) and used without further purification. The chemical identity of compounds was assessed by re-running Nuclear Magnetic Resonance spectroscopy (NMR) experiments and proved to be in agreement with the literature data reported for this compound. The purity, checked by reversed-phase High Performance Liquid Chromatography (HPLC), was approximately 95%. When not specified reagents and solvents were purchased from commercial suppliers (MERCK Life Science, TCI Chemicals, Eurisotop) and were used without further purification. UV/vis spectra were recorded on a Jasco V-750 spectrophotometer and fluorescence spectra were obtained using a Shimadzu RF-6000 spectrofluorophotometer. Melting points were recorded with Büchi melting point B-545 apparatus in open capillaries and are not corrected. NMR spectra have been acquired with a Bruker Avance/Ultra Shield™ 400 spectrometer operating at 400.13 MHz for ¹H and 100.62 MHz for ¹³C at room temperature, using tetramethylsilane (TMS) as internal standard and 5 mm diam-eter glass tubes. Chemical shifts (δ) are reported in parts per million (ppm) and coupling constants (J) in hertz (Hz), approximated to 0.1 Hz. The residual solvent peak was used as an internal reference for ¹H and ¹³C NMR spectra and is referenced to CD₂Cl₂ (δ = 5.26 ppm for ¹H, δ = 53.84 ppm for ¹³C). Data for ¹H NMR are reported as follows: chemical shift, multiplicity (br = broad, ovrlp = over-lapped, s = singlet, d = doublet, t = triplet, q =quartet, m = multiple, dd = doublet of doublets), coupling constant, integral. All ¹³C NMR spectra were obtained with complete proton decoupling. Spectra were processed with the pro-gram MestReNova version 12.0.0-20080, FT and zero filling at 64K. Chromatography was carried out on 60 Å silica gel (40-63 μ m, 230–400 mesh). All reactions were monitored by thin-layer chromatography (TLC), and 60 Å silica gel on TLC plates were used. The compounds on TLC were revealed by quenching fluorescence at 365 nm using a 4W UV lamp because the fluorescent markers of the invention are characterized by an excitation wavelength of 350 to 650 nm and an emission wavelength of 390 to 800 nm. Electron spray ionization mass spectra (ESI-MS) were performed on Bruker BioApex Fourier transform ioncyclotron resonance (FT-ICR) mass spectrometer.

Molecular modelling. Ligands were designed in 2D with PICTO version 4.4.0.4 (OpenEye Scientific Software, Santa Fe, NM)⁴³ and converted into 3D format by OMEGA version 3.1.0.3 (OpenEye Scientific Software, Santa Fe, NM)^{44,45}. The most prevalent ligand protonation form at pH 7.4 was assigned by QUACPAC version 2.0.0.3 (OpenEye Scientific Software, Santa Fe, NM)⁴⁶, while energy minimization was carried out by SZYBKI version 1.10.0.3 (OpenEye Scientific Software, Santa Fe, NM)⁴⁴ using the MMFF94S force field⁴⁷. The 6-mer model of the most conserved channel formed by four adjacent β -sheets was prepared as described in Verwilst et al,³¹ starting from the PDB-ID 5K7N⁴⁹. Molecular docking was carried out with AutoDock4.2 using default settings⁵⁰. Since common molecular modeling software such as OpeEye and AutoDock do not provide force field parameters for boron atoms, in our study it was replaced by a carbon atom having sp^3 hybridization.

Synthesis of 3. Trans-4-[2-(4-dimethylaminophenyl)vinyl]benzaldehyde was synthesized via Heck reaction starting from 4-bromobenzaldehyde (1) and 4-dimethylaminostyrene (2) according to a modified literature procedure¹¹. The suitable catalyst, chosen to promote the stereoselectivity of the reaction, was prepared in situ: 16.8 mg of palladium acetate (II) (0.075 mmol) and 19.7 mg of triphenylphosphine (0.075 mmol) have been soluble in DMF. After 10 minutes, a solution of 202 mg of 4-bromobenzaldehyde 1 (1.5 mmol), 264.6 mg of 4-dimethylaminostyrene 2 (1.8 mmol) and 414 mg of potassium carbonate (3.00 mmol) in 3 mL of DMF has been added to the catalyst solution. The reaction was left in agitation at 80°C for 4 h, after which 50 mL of a saturated NH_4Cl solution in water was added. Later, the mixture was extracted with CH_2Cl_2 (3 \times 100 mL) and the organic layers were combined, dried with Na_2SO_4 anhydrous and concentrated under vacuum. Compound 3 (1,074 mmol) was obtained by cold hexane crystallization as a yellow solid (270 mg, 72%). Mp: 218.0 – 220.0°C. ¹H NMR (400 MHz, CH_2Cl_2) δ 9.94 (s, 1H), 7.82 (d, J = 8.3 Hz, 2H), 7.62 (d, J = 8.3 Hz, 2H), 7.45 (d, J = 8.8 Hz, 2H), 7.23 (d, J = 16.3 Hz, 1H), 6.96 (d, J = 16.3 Hz, 1H), 6.72 (d, J = 8.8 Hz, 2H), 3.00 (s, 6H). ¹³C NMR (101 MHz, CH_2Cl_2) δ 191.3, 150.8, 144.5, 134.6, 132.4, 130.1, 128.1, 126.1, 124.5, 122.4, 112.3, 79.5, 40.1. ESI-MS(m/z): [M+H]⁺ calcd. For $C_{17}H_{18}NO$, 252.13; found 252.17

Synthesis of BT1. A solution of 100 mg (0.45 mmol) of commercially available 1, 112.95 mg (0.45 mmol) of compound 3, in the presence of 0.35 mL of acetic acid (3.5 mmol) and 0.35 mL of piperidine (6.12 mmol) in 10 mL of toluene was heated under Dean–Stark conditions for 4 h. The reaction was allowed to cool to room temperature, and 50 mL of a saturated aqueous NH_4Cl solution was added. The mixture was extracted with CH_2Cl_2 (3 \times 100 mL), and the organic layers were combined, dried over Na_2SO_4 anhydrous and concentrated at reduced pressure. Column chromatography (silica, EtOAc/hexane, 1:9 \rightarrow CH_2Cl_2) resulted in 18 mg (0.04 mmol, 18%) of BT1 as black solid. Mp: 257-262°C. ¹H NMR (400 MHz, CH_2Cl_2) δ 7.63-7.57 (m, 4H), 7.53 (d, J = 8.4 Hz, 2H), 7.46 – 7.42 (m, 3H), 7.23 (s, 1H), 7.16 (d, J = 16.4 Hz, 1H), 6.97 – 6.91 (m, 2H), 6.83 (bs, 1H), 6.72 (d, J = 8.9 Hz, 2H), 6.48-6.47 (m, 1H), 2.99 (s, 6H), 2.34 (s, 3H). ¹³C NMR (101 MHz, CH_2Cl_2) δ 151.4, 149.8, 141.2, 141.0, 139.0, 134.9, 131.3, 129.3, 128.9, 128.7, 127.2, 126.4, 125.9, 123.9, 123.6, 121.3, 118.2, 118.1, 117.0, 113.1, 41.0, 12.1. ESI-MS(m/z): [M+H]⁺ calcd. For $C_{28}H_{27}BF_2N_3$, 453.22; found 454.33.

Human iPSCs Maintenance. Induced pluripotent stem cell line (WT#1)^{39,40} was maintained in mTeSR Plus medium (STEMCELL Technologies) on growth factor-reduced Matrigel-coated (Corning; dilution 1:100) plates at 37°C in 5% CO₂ and iPSC colonies were passaged with PluriS-TEM Dispase-II (Merck Life Science) when 80% confluent.

iPSCs Differentiation to cortical neurons. iPSC WT#1 was differentiated with a two-step protocol based on doxycycline-induced expression of human NGN2 transcript as previously described. Briefly, human iPSC cells were treated with 1X Accutase (Thermo Fisher Scientific) and plated onto growth factor-reduced Matrigel-coated plates at a density of 1000 cells/mm² in mTeSR Plus containing 10 µM Rock-inhibitor Y-27632 (STEMCELL Technologies) and 2 µg/mL doxycycline (Merck Life Science). The day of seeding is set as day minus 3 (D-3). One day after seeding (D-2), the medium is switched to N2 medium consisting of DMEM/F12 [1:1], 1% N2 supplement, 1% NEAA, 1% GlutaMAX (Thermo Fisher Scientific) supplemented with 2 µg/mL doxycycline (Merck Life Science) to sustain human NGN2 expression. N2 medium was refreshed every day. Three days after (D0), the early born neurons were dissociated with Accutase and plated onto PDL/laminin-coated (Merck Life Science) dishes at a density of 500 cells/mm² in maturation medium consisting of Neurobasal, 2% B27 with vitamin A, 1% GlutaMAX (Thermo Fisher Scientific), 0,5 µg/mL laminin (Merck Life Science), 20 ng/mL BDNF (Peprotech), 20 ng/mL ascorbic acid (Peprotech), 10 ng/mL GDNF (Peprotech) supplemented with 2 µg/mL doxycycline, 10 µM Rock-inhibitor Y-27632 and 10 µM DAPT (STEMCELL Technologies). After 24 hours, doxycycline and Y-27632 were removed and the medium was refreshed every three days until day 10. Optionally, 2 µM Ara-C (Merck Life Science) was added to the medium on day 4 and day 7 to remove proliferative cells. Thereafter, the maturation medium was half changed weekly until the experimental window was reached around D30.

RT-PCR and RT-qPCR. Total RNA was extracted with the EZNA Total RNA Kit I (Omega Bio-Tek) and retrotranscribed using the iScript Reverse Transcription Supermix for RT-qPCR (Bio-Rad). Real-time RT-PCR was performed with iTaq Universal SYBR Green Supermix (Bio-Rad) on a ViiA 7 Real-Time PCR System (Applied Biosystems) and housekeeping gene ATP5O (ATP synthase, H⁺ transporting, mitochondrial F1 complex, O sub-unit) was used as an internal control. A complete list of primers is provided in the supplementary material (Supplementary Table 3).

Induction of a tau hyperphosphorylated state and staining with BODIPY-base probes. iPSC-derived cortical networks were treated with 50 nM Okadaic acid (OA; Merck Life Science) for 2 hours at 37°C in 5% CO₂. Afterward, untreated and treated neuronal cultures were incubated with either 100 µM TAU1 probe or 100 µM BT1 probe for 30 minutes at 37°C and thus fixed for 15 minutes at room temperature with cool and fresh-made 4% PFA.

Immunostaining. Fixed iPSC-derived cortical neurons were permeabilized with 0.2% Triton X-100 (Merck Life Science) in 1X TBS and incubated for 1 hour in blocking solution containing 1X TBS, 0.2% Triton X-100, and 5% goat serum (Merck Life Science). Afterwards, the cells were incubated in blocking solution containing primary antibodies overnight at 4°C. The primary antibodies employed in this study were anti PHF-tau Ser202/Thr205 (AT8; dilution 1:200; Thermo Fisher Scientific) and anti-oligomeric tau (T22;

dilution 1:200; Merck Life Science) followed by incubation with secondary antibody (dilution 1:1000) for 1 hour at room temperature. A complete list of antibodies is provided in the supplementary material (Supplementary Table 2).

Images were acquired with an inverted microscope equipped with the X-Light V2 Spinning Disk Confocal module (Crest Optics) with a 40×/NA 0.75 objective lens in stack with z-step of 0.4 μm . Image processing was performed through custom numeric codes implemented in MATLAB environment.

Image analysis. Image processing was performed through custom numeric codes implemented in MATLAB environment. The algorithm consists of three main steps: image correction, image binarization and colocalization.

Correction (Figure 6A). For each channel, the maximum z-projection obtained from the z-stack was examined. Noise and background affecting each channel were removed before carrying out the quantitative analysis. A moving average filter (5x5 pixels window) was used to reduce the noise, the background affecting each channel was automatically retrieved and subtracted through the statistical analysis of global pixel intensity distribution (negative values have been set to zero). More precisely, a histogram shape-based method was used, which identifies background levels beyond the peaks of the smoothed histograms. Furthermore, to exclude unwanted signals, a neurite structure mask, obtained by thresholding pixel values on the AT8 channel, was applied to each channel.

Binarization (Figure 6B) Meaningful pixels were selected for each corrected image. For this purpose, removing background and thresholding, unfortunately, was not sufficient: low threshold values lead to an overestimation of the signal, and higher values could cause information loss. To overcome this problem, the following iterative procedure was designed. Starting from a low threshold value, 20% of the maximum signal, at each step the threshold was increased by 15%, until enough pixels were no longer selected. A different binary image was obtained for each threshold: the final binary image was obtained by combining them and deleting the largest of the overlapping areas (more than 70% overlapping). Finally, the area covered by the fluorescence signal and the corresponding integrated density were calculated for each channel.

Colocalization (Figure 6C) To quantify the colocalization of the probe with the anti-bodies T22 and AT8 the following procedure was followed. Two of the most used colocalization coefficients were exploited: Pearson's correlation coefficient (PC) and Manders' overlap coefficient (M1), which measure correlation and co-occurrence respectively. An easy way to visualize the dependence of pixels in dual-channel images is to consider a pixel distribution diagram called scatter plot or fluorogram (orange and green plots in Figure 6C), where x-coordinates are given by the pixel intensities of the probe image and y-coordinates are given by the pixel intensities of the antibody image. This scatter plot provides the first intuitive evidence of colocalization: in a complete colocalization the points on the diagram are distributed around a line (e.g. green plot in Figure 5C) and the spread with respect to the line is measured by the correlation coefficient PC. More precisely, PC quantifies pixel intensity spatial correlation and, being calculated on corrected not binary images, it is independent of the binarization step. However, in a more

general scenario (e.g. orange plot in Figure 5C), in addition to scatter plots and PC it is necessary to evaluate colocalization by using the corrected binary images and calculating the coefficient M1. M1 is defined as the ratio of the 'summed intensities of pixels from the antibody image for which the intensity in the probe channel is above zero' to the 'total intensity in the antibody channel'. Hence M1 measures the fraction of antibody signal coinciding with probe signal, an ideal tool to quantify probes efficiency. PC and M1 can be considered reliable colocalization coefficients since images were properly corrected, similar acquisition and thresholding conditions were applied, and a large set of images was compared.

Statistical data analysis. Statistical analysis, graphs and plots were generated using GraphPad Prism 6 (GraphPad Software) and MATLAB 2016b (MathWorks). To verify whether our data sets were reflecting normal distribution, the Shapiro-Wilk normality test was performed. Where the normality distribution was not fulfilled, statistical significance analysis was performed using the non-parametric two-sided Mann-Whitney test (MW test, $P=0.05$). In all other cases, whether not stated otherwise, t-Student test ($P=0.05$) was performed, and data set are given as mean \pm standard error of the mean (s.e.m.).

Declarations

Acknowledgments

MM wish to thank the OpenEye Free Academic Licensing Programme for providing a free academic licence for molecular modelling and chemoinformatics software. The authors wish to thank the Center for Life Nano and Neuro Science Imaging Facility, Istituto Italiano di Tecnologia.

This research was funded by the CrestOptics-IIT JointLab for Advanced Microscopy (to S.D.A., A.B, and F.G.), and the MARBEL Life2020 grant (to S.D.A. and A.B). This work was partially supported by Sapienza University (to S.D.A. RM118163E0297F84; PH12017270934C3C) and Fondazione Istituto Italiano di Tecnologia. The work was financially supported by the Excellence Departments grant from MIUR (Art. 1, commi 314-337 Legge 232/2016) to the Department of Chemistry and Technology of Drugs. This work was also partially supported by PON (Piano Operativo Nazionale) Grant ARS01_00432 PROGEMA, "Processi Green per l'Estrazione di Principi Attivi e la Depurazione di Matrici di Scarto e Non", 03/2018-09/ 2020. M.A. has been supported by MIUR - Ministero dell'Istruzione Ministero dell'Università e della Ricerca (Ministry of Education, University and Research) under the national project FSE/FESR - PON Ricerca e Innovazione 2014-2020 (N° AIM1887574, CUP: E18H19000350007). P.B. and F.G. has been supported from Regione LAZIO, Lazio-Innova, POR FESR Lazio 2014-2020, European Union in the form of Grant A0375-2020-36549 CUP B85F20003340002 (www.europa.eu; www.lazioeuropa.it). S.D.A. was supported from Bio3DBrain FSE 2014-2020 Regione Lazio. The research leading to these results has been also supported by European Research Council Synergy grant ASTRA (n. 855923 to G.C.R.).

Author contributions statement

A.B., F.G. and S.D.A. conceived the experiments, A.S., D.Q. P.B., I.R., M.A. C.P., I.S. A.I., and R.I. conducted the experiments, M.M. and B.B. conducted the models, S.G., F.G., and P.B. analyzed the results. S.D.A., F.G.,

and A.B. wrote the article with the help of A.S., G.C.R. and P.B. All authors reviewed the manuscript. A.B., F.G. and S.D.A. conceived the project. All authors have given approval to the final version of the manuscript. A.S. and D.Q. contributed equally.

Data Availability Statement

The data that support the findings of this study are available from the corresponding author upon reasonable request.

Additional information

The authors declare no competing financial interest.

References

1. Graham, W. V.; Bonito-Oliva, A.; Sakmar, T. P., Update on Alzheimer's disease therapy and prevention strategies. *Annual review of medicine* 2017, 68, 413-430.
2. Masters, C.; Bateman, R.; Blennow, K.; Rowe, C., Sperling 432 RA, Cummings JL, Alzheimer's disease. *Nat Rev Dis 433 Primers* 2015, 1 (15056), 434.
3. Delacourte, A.; Sergeant, N.; Wattez, A.; Gauvreau, D.; Robitaille, Y., Vulnerable neuronal subsets in Alzheimer's and Pick's disease are distinguished by their τ isoform distribution and phosphorylation. *Annals of Neurology: Official Journal of the American Neurological Association and the Child Neurology Society* 1998, 43 (2), 193-204.
4. Olsson, B.; Lautner, R.; Andreasson, U.; Öhrfelt, A.; Portelius, E.; Bjerke, M.; Hölttä, M.; Rosén, C.; Olsson, C.; Strobel, G., CSF and blood biomarkers for the diagnosis of Alzheimer's disease: a systematic review and meta-analysis. *The Lancet Neurology* 2016, 15 (7), 673-684.
5. Pietrzak, K.; Czarnecka, K.; Mikiciuk-Olasik, E.; Szymanski, P., New perspectives of Alzheimer disease diagnosis—The most popular and future methods. *Medicinal Chemistry* 2018, 14 (1), 34-43.
6. Jack Jr, C. R.; Bennett, D. A.; Blennow, K.; Carrillo, M. C.; Dunn, B.; Haeberlein, S. B.; Holtzman, D. M.; Jagust, W.; Jessen, F.; Karlawish, J., NIA-AA research framework: toward a biological definition of Alzheimer's disease. *Alzheimer's & Dementia* 2018, 14 (4), 535-562.
7. Hardy, J.; Selkoe, D. J., The amyloid hypothesis of Alzheimer's disease: progress and problems on the road to therapeutics. *Science* 2002, 297 (5580), 353-356.
8. Barone, E., Brain insulin resistance: an early risk factor for Alzheimer's disease development in Down syndrome. *Neural Regeneration Research* 2021, 17 (2), 333.
9. Bryan Jr, A. W.; Menke, M.; Cowen, L. J.; Lindquist, S. L.; Berger, B., BETASCAN: probable β -amyloids identified by pairwise probabilistic analysis. *PLoS computational biology* 2009, 5 (3), e1000333.
10. Oddo, S.; Caccamo, A.; Shepherd, J. D.; Murphy, M. P.; Golde, T. E.; Kaye, R.; Metherate, R.; Mattson, M. P.; Akbari, Y.; LaFerla, F. M., Triple-transgenic model of Alzheimer's disease with plaques and tangles: intracellular A β and synaptic dysfunction. *Neuron* 2003, 39 (3), 409-421.

11. Grimaldi, A.; Brighi, C.; Peruzzi, G.; Ragozzino, D.; Bonanni, V.; Limatola, C.; Ruocco, G.; Di Angelantonio, S., Inflammation, neurodegeneration and protein aggregation in the retina as ocular biomarkers for Alzheimer's disease in the 3xTg-AD mouse model. *Cell Death & Disease* 2018, 9 (6), 1-10.
12. Ostrowitzki, S.; Deptula, D.; Thurfjell, L.; Barkhof, F.; Bohrmann, B.; Brooks, D. J.; Klunk, W. E.; Ashford, E.; Yoo, K.; Xu, Z.-X., Mechanism of amyloid removal in patients with Alzheimer disease treated with gantenerumab. *Archives of neurology* 2012, 69 (2), 198-207.
13. Giacobini, E.; Gold, G., Alzheimer disease therapy—moving from amyloid- β to tau. *Nature Reviews Neurology* 2013, 9 (12), 677-686.
14. Doody, R. S.; Thomas, R. G.; Farlow, M.; Iwatsubo, T.; Vellas, B.; Joffe, S.; Kieburtz, K.; Raman, R.; Sun, X.; Aisen, P. S., Phase 3 trials of solanezumab for mild-to-moderate Alzheimer's disease. *New England Journal of Medicine* 2014, 370 (4), 311-321.
15. Salloway, S.; Sperling, R.; Fox, N. C.; Blennow, K.; Klunk, W.; Raskind, M.; Sabbagh, M.; Honig, L. S.; Porsteinsson, A. P.; Ferris, S., Two phase 3 trials of bapineuzumab in mild-to-moderate Alzheimer's disease. *New England Journal of Medicine* 2014, 370 (4), 322-333.
16. Edison, P.; Archer, H.; Hinz, R.; Hammers, A.; Pavese, N.; Tai, Y.; Hotton, G.; Cutler, D.; Fox, N.; Kennedy, A. J. N., Amyloid, hypometabolism, and cognition in Alzheimer disease: an [11C] PIB and [18F] FDG PET study. *Neurology* 2007, 68 (7), 501-508.
17. Li, H.; Wetten, S.; Li, L.; Jean, P. L. S.; Upmanyu, R.; Surh, L.; Hosford, D.; Barnes, M. R.; Briley, J. D.; Borrie, M., Candidate single-nucleotide polymorphisms from a genomewide association study of Alzheimer disease. *Archives of neurology* 2008, 65 (1), 45-53.
18. Chételat, G.; La Joie, R.; Villain, N.; Perrotin, A.; de La Sayette, V.; Eustache, F.; Vandenberghe, R., Amyloid imaging in cognitively normal individuals, at-risk populations and preclinical Alzheimer's disease. *NeuroImage: Clinical* 2013, 2, 356-365.
19. Dickson, D.; Ksiazak-Reding, H.; Liu, W.-K.; Davies, P.; Crowe, A.; Yen, S.-H., Immunocytochemistry of neurofibrillary tangles with antibodies to subregions of tau protein: identification of hidden and cleaved tau epitopes and a new phosphorylation site. *Acta neuropathologica* 1992, 84 (6), 596-605.
20. Villemagne, V. L.; Okamura, N., Tau imaging in the study of ageing, Alzheimer's disease, and other neurodegenerative conditions. *Current opinion in neurobiology* 2016, 36, 43-51.
21. Leuzy, A.; Chiotis, K.; Lemoine, L.; Gillberg, P.-G.; Almkvist, O.; Rodriguez-Vieitez, E.; Nordberg, A., Tau PET imaging in neurodegenerative tauopathies—still a challenge. *Molecular psychiatry* 2019, 24 (8), 1112-1134.
22. Verwilt, P.; Kim, H. S.; Kim, S.; Kang, C.; Kim, J. S., Shedding light on tau protein aggregation: the progress in developing highly selective fluorophores. *Chemical Society Reviews* 2018, 47 (7), 2249-2265.
23. Yuksel, M.; Tacal, O., Trafficking and proteolytic processing of amyloid precursor protein and secretases in Alzheimer's disease development: An up-to-date review. *European journal of pharmacology* 2019, 856, 172415.

24. Jun, Y. W.; Cho, S. W.; Jung, J.; Huh, Y.; Kim, Y.; Kim, D.; Ahn, K. H., Frontiers in probing Alzheimer's disease biomarkers with fluorescent small molecules. *ACS central science* 2019, 5 (2), 209-217.
25. Kolb, H. C.; Andrés, J. I., Tau positron emission tomography imaging. *Cold Spring Harbor perspectives in biology* 2017, 9 (5), a023721.
26. Elbatrawy, A. A.; Hyeon, S. J.; Yue, N.; Osman, E. E. A.; Choi, S. H.; Lim, S.; Kim, Y. K.; Ryu, H.; Cui, M.; Nam, G., "Turn-On" Quinoline-Based Fluorescent Probe for Selective Imaging of Tau Aggregates in Alzheimer's Disease: Rational Design, Synthesis, and Molecular Docking. *ACS sensors*
27. Fitzpatrick, A. W.; Falcon, B.; He, S.; Murzin, A. G.; Murshudov, G.; Garringer, H. J.; Crowther, R. A.; Ghetti, B.; Goedert, M.; Scheres, S. H., Cryo-EM structures of tau filaments from Alzheimer's disease. *Nature* 2017, 547 (7662), 185-190.
28. Kellogg, E. H.; Hejab, N. M.; Poepsel, S.; Downing, K. H.; DiMaio, F.; Nogales, E., Near-atomic model of microtubule-tau interactions. *Science* 2018, 360 (6394), 1242-1246.
29. Pizzarelli, R.; Pediconi, N.; Di Angelantonio, S., Molecular Imaging of Tau Protein: New Insights and Future Directions. *Frontiers in Molecular Neuroscience* 2020, 13, 233.
30. Durantini, A. M.; Heredia, D. A.; Durantini, J. E.; Durantini, E. N., BODIPYs to the rescue: Potential applications in photodynamic inactivation. *European journal of medicinal chemistry* 2018, 144, 651-661.
31. Verwilt, P.; Kim, H.-R.; Seo, J.; Sohn, N.-W.; Cha, S.-Y.; Kim, Y.; Maeng, S.; Shin, J.-W.; Kwak, J. H.; Kang, C., Rational design of in vivo tau tangle-selective near-infrared fluorophores: expanding the BODIPY universe. *Journal of the American Chemical Society* 2017, 139 (38), 13393-13403.
32. Schön, C.; Hoffmann, N. A.; Ochs, S. M.; Burgold, S.; Filser, S.; Steinbach, S.; Seeliger, M. W.; Arzberger, T.; Goedert, M.; Kretschmar, H. A., Long-term in vivo imaging of fibrillar tau in the retina of P301S transgenic mice. *PLoS One* 2012, 7 (12), e53547.
33. den Haan, J.; Janssen, S. F.; van de Kreeke, J. A.; Scheltens, P.; Verbraak, F. D.; Bouwman, F. H., Retinal thickness correlates with parietal cortical atrophy in early-onset Alzheimer's disease and controls. *Alzheimer's Dementia: Diagnosis, Assessment Disease Monitoring* 2018, 10, 49-55.
34. Grimaldi, A.; Pediconi, N.; Oieni, F.; Pizzarelli, R.; Rosito, M.; Giubettini, M.; Santini, T.; Limatola, C.; Ruocco, G.; Ragozzino, D., Neuroinflammatory processes, A1 astrocyte activation and protein aggregation in the retina of Alzheimer's disease patients, possible biomarkers for early diagnosis. *Frontiers in neuroscience* 2019, 13, 925.
35. Gupta, V. B.; Chitranshi, N.; den Haan, J.; Mirzaei, M.; You, Y.; Lim, J. K.; Basavarajappa, D.; Godinez, A.; Di Angelantonio, S.; Sachdev, P., Retinal changes in Alzheimer's disease—integrated prospects of imaging, functional and molecular advances. *Progress in retinal and eye research* 2021, 82, 100899.
36. Ngolab, J.; Honma, P.; Rissman, R. A., Reflections on the utility of the retina as a biomarker for Alzheimer's disease: a literature review. *Neurology and therapy* 2019, 8 (2), 57-72.
37. Laurijssens, B.; Aujard, F.; Rahman, A., Animal models of Alzheimer's disease and drug development. *Drug Discovery Today: Technologies* 2013, 10 (3), e319-e327.

38. Sandoe, J.; Eggan, K., Opportunities and challenges of pluripotent stem cell neurodegenerative disease models. *Nature neuroscience* 2013, 16 (7), 780-789.
39. Lenzi J, De Santis R, de Turris V, Morlando M, Laneve P, Calvo A, Caliendo V, Chiò A, Rosa A, Bozzoni I. ALS mutant FUS proteins are recruited into stress granules in induced pluripotent stem cell-derived motoneurons. *Dis Model Mech.* 2015 Jul 1;8(7):755-66.
40. Brighi C, Salaris F, Soloperto A, Cordella F, Ghirga S, de Turris V, Rosito M, Porceddu PF, D'Antoni C, Reggiani A, Rosa A, Di Angelantonio S. Novel fragile X syndrome 2D and 3D brain models based on human isogenic FMRP-KO iPSCs. *Cell Death Dis.* 2021 May 15;12(5):498.
41. Zhang, Y.; Pak, C.; Han, Y.; Ahlenius, H.; Zhang, Z.; Chanda, S.; Marro, S.; Patzke, C.; Acuna, C.; Covy, J., Rapid single-step induction of functional neurons from human pluripotent stem cells. *Neuron* 2013, 78 (5), 785-798.
42. Li Y , Wang K , Zhou K , Guo W , Dai B , Liang Y , Dai J , Cui M . Novel D-A-D based near-infrared probes for the detection of β -amyloid and Tau fibrils in Alzheimer's disease. *Chem Commun (Camb).* 2018 Aug 2;54(63):8717-8720.
43. PICTO 4.4.0.4: OpenEye Scientific Software, Santa Fe, NM. <http://www.eyesopen.com>.
44. OMEGA 3.1.0.3: OpenEye Scientific Software, Santa Fe, NM. <http://www.eyesopen.com>.
45. Hawkins, P. C.; Skillman, A. G.; Warren, G. L.; Ellingson, B. A.; Stahl, M. T., Conformer generation with OMEGA: algorithm and validation using high quality structures from the Protein Databank and Cambridge Structural Database. *Journal of chemical information modeling* 2010, 50 (4), 572-584.
46. QUACPAC 2.0.0.3: OpenEye Scientific Software, Santa Fe, NM. <http://www.eyesopen.com>.
47. SZYBKI 1.10.0.3: OpenEye Scientific Software, Santa Fe, NM. <http://www.eyesopen.com>.
48. Halgren, T. A. MMFF VI. MMFF94s Option for Energy Minimization Studies. *Comput. Chem.* 1999, 20, 720-729
49. de la Cruz, M. J.; Hattne, J.; Shi, D.; Seidler, P.; Rodriguez, J.; Reyes, F. E.; Sawaya, M. R.; Cascio, D.; Weiss, S. C.; Kim, S. K., Atomic-resolution structures from fragmented protein crystals with the cryoEM method MicroED. *Nature methods* 2017, 14 (4), 399-402.
50. Morris, G. M.; Huey, R.; Lindstrom, W.; Sanner, M. F.; Belew, R. K.; Goodsell, D. S.; Olson, A. J., AutoDock4 and AutoDockTools4: Automated docking with selective receptor flexibility. *Journal of computational chemistry* 2009, 30 (16), 2785-2791.

Figures

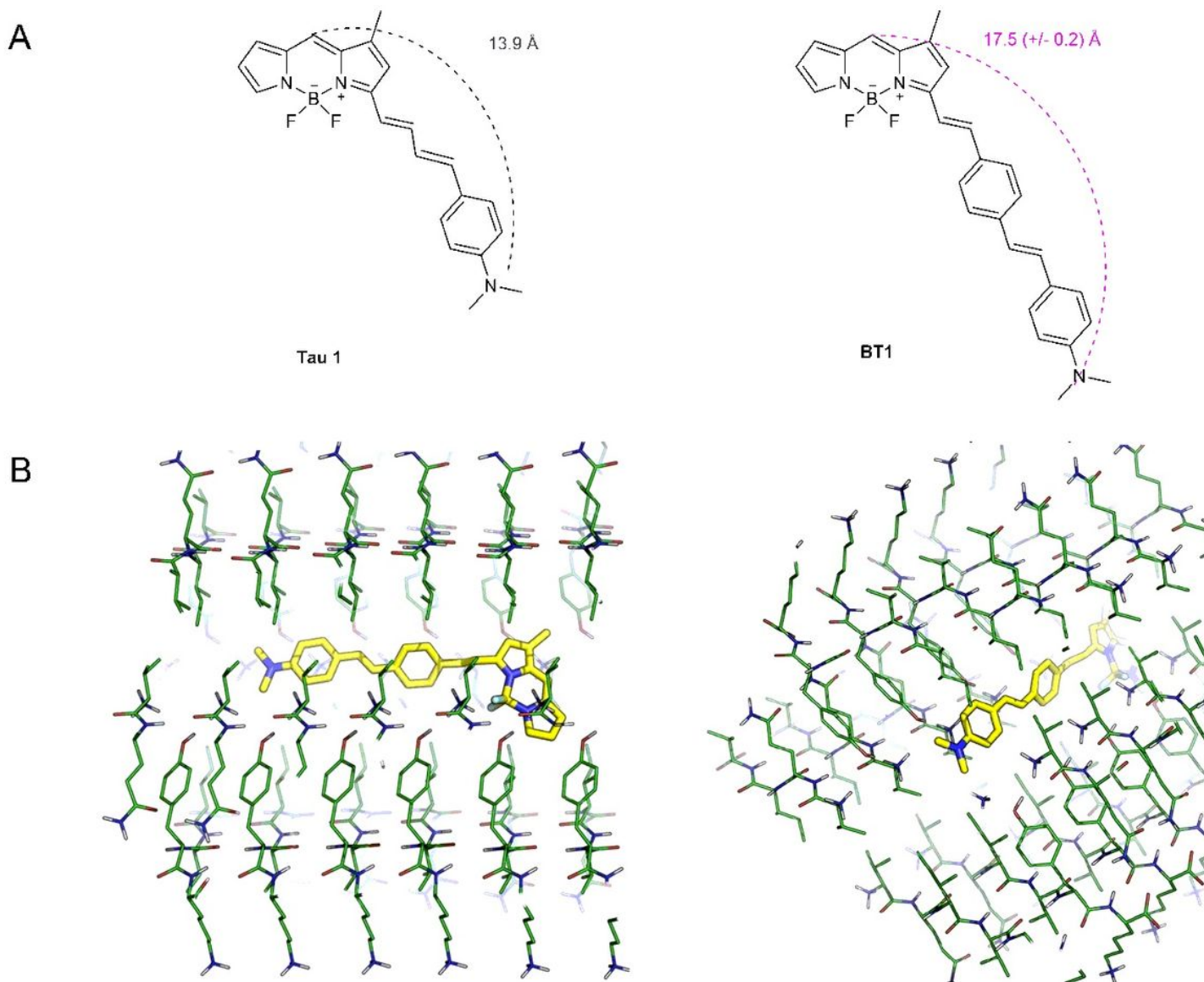


Figure 1

Chemical structures of BODIPY based fluorophores. (A) Chemical structures of TAU1 and BT1. (B) Molecular docking of BT1 against the crystallographic structure of the PHF6 fragment: side and diagonal view of the molecule in the protein tunnel.

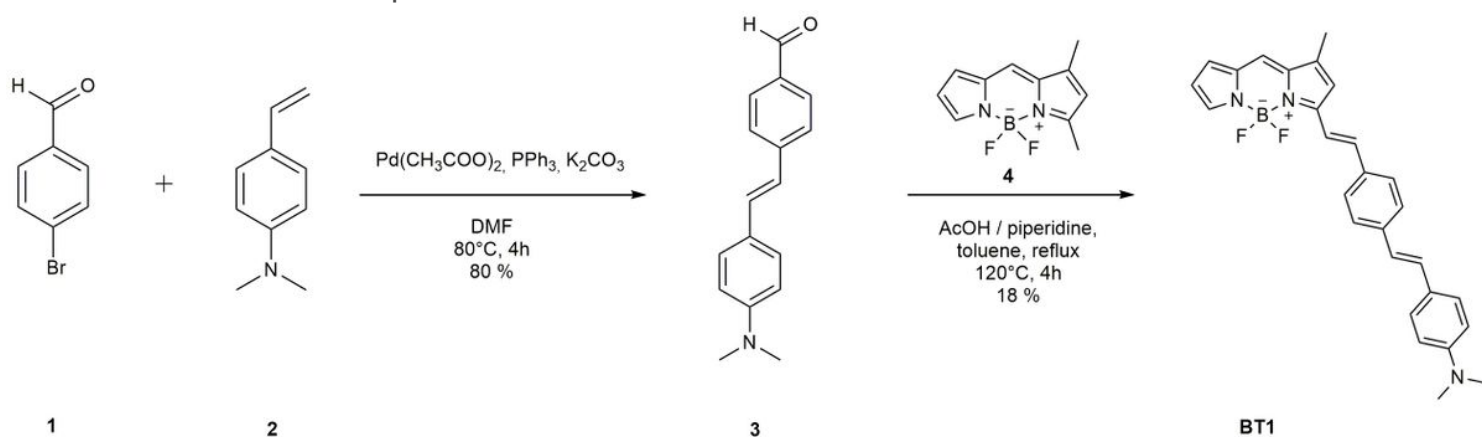


Figure 2

Two-step synthetic strategy for the preparation of BT1.

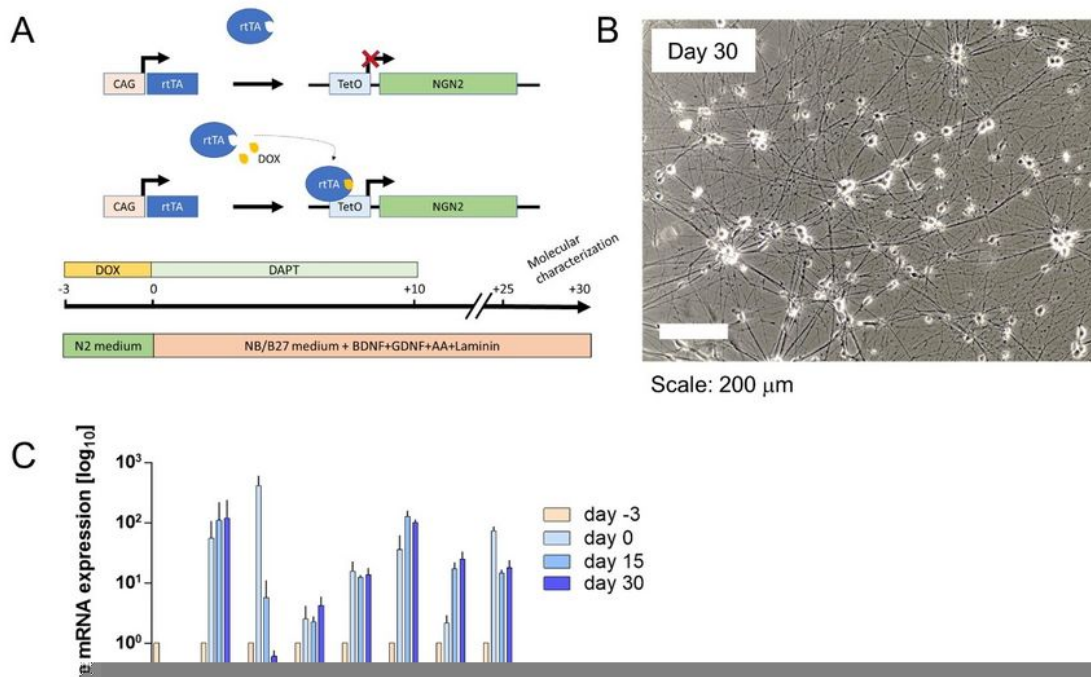


Figure 3

Molecular and cellular characterization of human iPSC derived NGN2 cortical neurons. (A) Schematic representation of the doxycycline-based strategy used for inducing the tuned expression of human NGN2

transcript. (B) Representative transmitted image of human iPSC-derived cortical neurons at day 30 in vitro. Scale bar 200 μm . (C) Real-time qRT-PCR analysis of specific molecular markers expression in human iPSC-derived cortical neurons at different time points of differentiation (n = 3 differentiation batches). (D) Representative images of immunostaining for NeUN (red), and MAP2 (green) expression in human iPSC-derived cortical neurons at day 30. Nuclei are stained in blue. Scale bar: 100 μm . (E) Representative images of immunostaining for total tau protein (HT7, red), and TUJ1 (green) expression in human iPSC-derived cortical neurons at day 30. Nuclei are stained in blue. Scale bar: 100 μm .

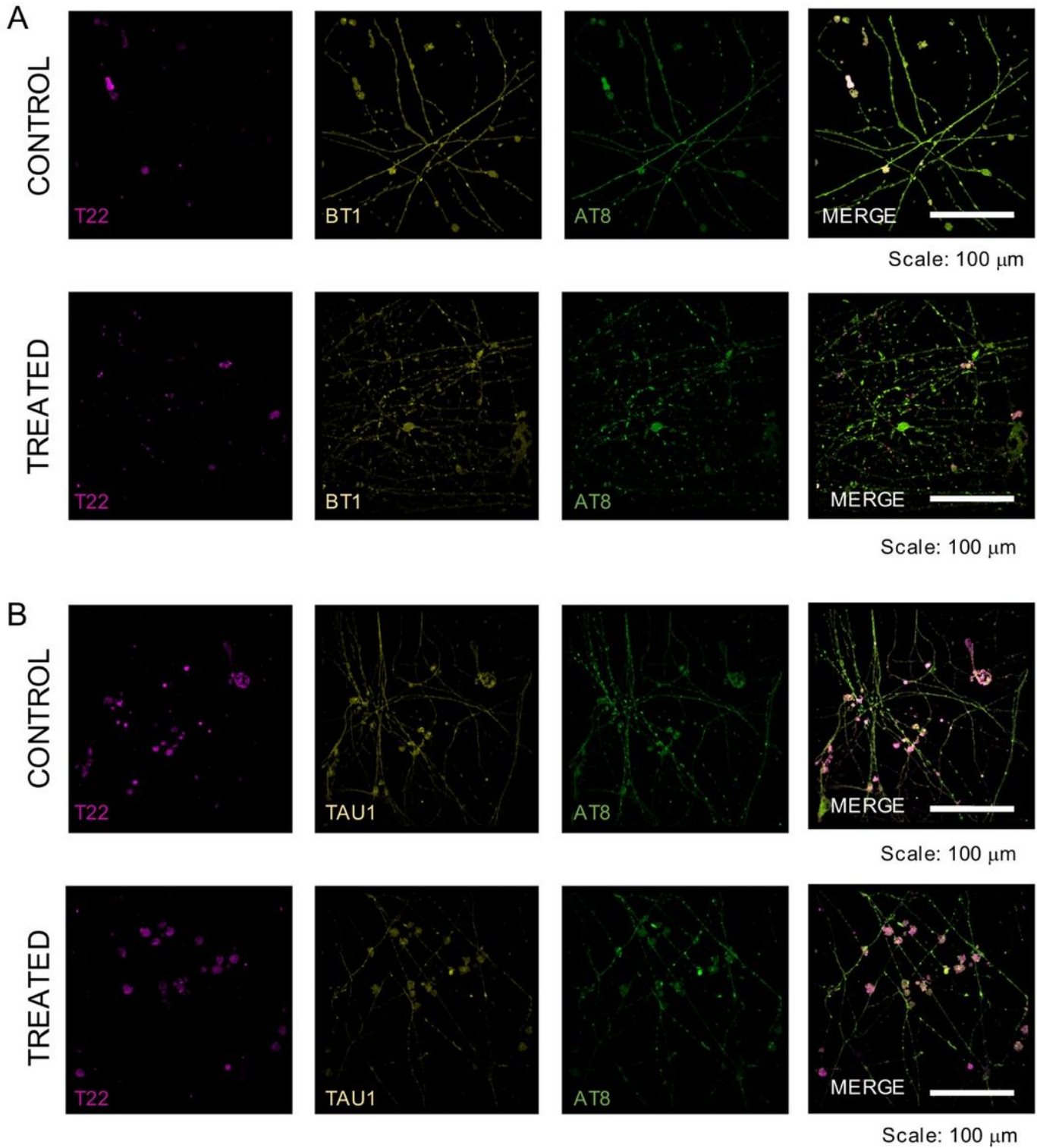


Figure 4

BT1 and TAU1 staining of hyperphosphorylated tau in iPSCs derived cortical neurons. (A) Top: Representative fluorescence images of control human iPSC-derived cortical neurons at 30 days in vitro incubated with BT1 (100 μ M) for 30 min at 37 $^{\circ}$ C and then stained for AT8 (green) and T22 (magenta). Bottom: Representative fluorescence images of human iPSC-derived cortical neurons treated with okadaic acid (50 nM) for 2 h before incubation with BT1 (100 μ M) for 30 min at 37 $^{\circ}$ C and relative staining for AT8 (green) and T22 (magenta). Images were acquired on an Olympus iX73 microscope equipped with an X-Light V3 spinning disc head using a 40x magnification. Scale bar: 100 μ m. (B) Top: Representative fluorescence images of control human iPSC-derived cortical neurons at 30 days in vitro incubated with TAU1 (100 μ M) for 30 min at 37 $^{\circ}$ C and then stained for AT8 (green) and T22 (magenta). Bottom: Representative fluorescence images of human iPSC-derived cortical neurons treated with okadaic acid (50 nM) for 2 h before incubation with TAU1 (100 μ M) for 30 min at 37 $^{\circ}$ C and relative staining for AT8 (green) and T22 (magenta). Images were acquired on an Olympus iX73 microscope equipped with an X-Light V3 spinning disc head using a 40x magnification. Scale bar: 100 μ m.

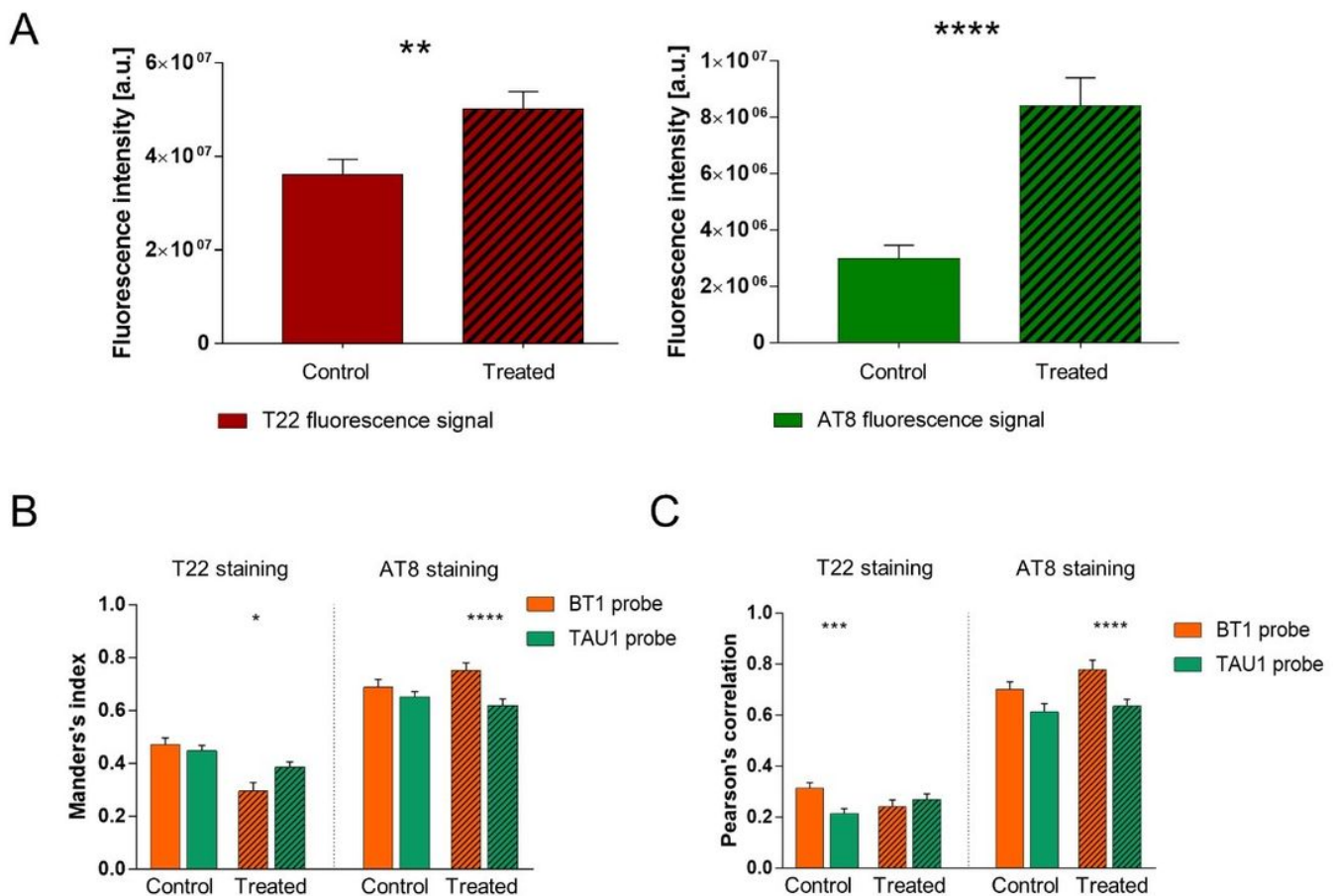


Figure 5

BT1 binds to hyperphosphorylated and oligomeric tau in OA treated neurons. (A) Bar charts showing the fluorescence intensity quantification of (left) T22 signal (** $p = 0.002$, MW test; $n = 53/3$, fields of view/batches) and (right) AT8 signals (**** $p < 0.0001$, MW test; $n = 53/6/3$, fields of view/batches) in control condition and after the treatment with okadaic acid (50 nM) for 2 h. (B) Left, Manders's colocalization in-dex of T22 staining with TAU1 (green) and BT1 (orange) fluorescence signal in control condition ($p = 0.48$, t-test; $n = 25/3$, fields of view/batches) and after the treatment with okadaic acid (50 nM) for 2 h (* $p < 0.017$, MW test; $n = 25/3$, fields of view/batches). Right, Manders's colocalization index of AT8 staining with TAU1 (green) and BT1 (orange) fluorescence signal in control condition ($p = 0.408$, MW test; $n = 25/3$, fields of view/batches) and after the treatment with okadaic acid (50 nM) for 2 h (**** $p < 0.0001$, MW test; $n = 25/3$, fields of view/batches), as determined using the custom-made MATLAB code. (C) On the left, Pearson's correlation index of T22 staining with TAU1 (green) and BT1 (orange) fluorescence signal in control condition (*** $p = 0.0008$, t-test; $n = 25/3$, fields of view/batches) and after the treatment with okadaic acid (50 nM) for 2 h ($p = 0.423$, t-test; $n = 25/3$, fields of view/batches). On the right, Pearson's correlation index of AT8 staining with TAU1 (green) and BT1 (orange) fluorescence signal in control condition ($p = 0.056$, MW test; $n = 25/3$, fields of view/batches) and after the treatment with okadaic acid (50 nM) for 2 h (**** $p < 0.0001$, MW test; $n = 25/3$, fields of view/batches), as determined using the custom-made MATLAB code.

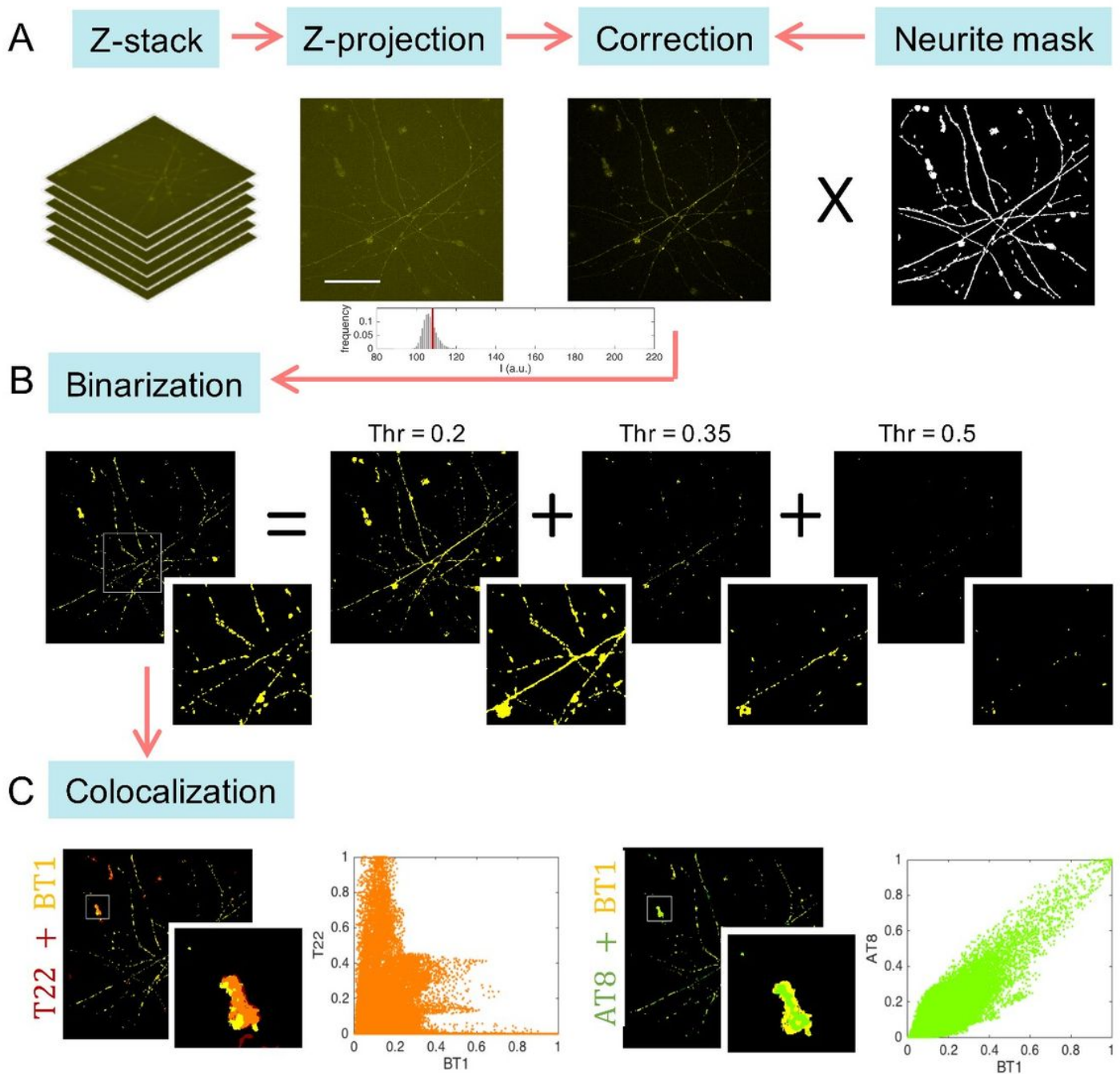


Figure 6

Schematic representation of MATLAB based algorithm for image analysis. (A) The maximum z-projection is calculated for each z-stack, then the background level is automatically retrieved and subtracted. The neurite structure mask is de-fined and applied as a filter to exclude unwanted signals located not in neurite structures. (B) An iterative thresholding procedure is used to binarized the image. Starting from the threshold value Thr=0.2 (20 % of the maximum signal) at each iteration, the threshold limit is increased by 0.15 units. The entire threshold image collection is combined to get a well-resolved binarized image. (C) The colocalization of the probe (BT1) with the antibodies (T22 and AT8) is calculated. Two

well-known colocalization methods are exploited: the scatter plots (orange and green), which allow visualizing the correlation measured by PC coefficient, and the merged binary images (red/yellow and green/yellow), which allow to visualize the co-occurrence measured by M1 coefficient.

Supplementary Files

This is a list of supplementary files associated with this preprint. Click to download.

- [SolopertoetalSupplementaryInformations.pdf](#)